Regular Article

PHYSICAL CHEMISTRY RESEARCH
Published by the
Iranian Chemical Society
www.physchemres.org
info@physchemres.org

Phys. Chem. Res., Vol. 8, No. 1, 175-202, March 2020
DOI: 10.22036/pcr.2019.201520.1676

Synthesis of CuO/MCM-41 Photocatalyst Nanocomposite, Mechanistic Study and Optimization of Quinoline Oxidative Degradation without Auxiliary Oxidant Using Response Surface Methodology

M. Kamani, R. Fazaeli*, M. Arjmand and M.H. Ghorbani
Department of Chemistry, South Tehran Branch, Islamic Azad University, Tehran, 11365-4435, Iran
(Received 14 September 2019, Accepted 2 January 2020)

Along with the development of science and technology, the attention of researchers has been drawn to the use of catalysts for removing pollutants from oil. In this research, the oxidative degradation of quinoline using CuO/MCM-41 nanoparticles was optimized in the presence of ultraviolet radiation without any auxiliary oxidants using Response Surface Methodology (RSM). The CuO/MCM-41 nanocomposite was synthesized by applying a facile method and was investigated using XRD, FESEM, EDS, mapping, FTIR and BET/BJH techniques. The degradation efficiency was measured by a UV spectrophotometer, and was evaluated by the use of GC-MASS technique. The results indicated that the highest removal of quinoline without using auxiliary oxidant and with the help of synthetic catalyst was about 84%.

Keywords: MCM-41, Photocatalyst nanocomposite, Quinoline, Oxidative degradation, Response surface methodology

INTRODUCTION

Since the application of liquid fuels is very popular in transportation, this has resulted in the production of 95% of the world's transport fuel from crude oil [1,2]. Producing nitrogen and sulfur oxides in the atmosphere results from the presence of these compounds in the fuel. Consequently, despite having many benefits, atmospheric pollution becomes a serious problem for the environment and ecosystems and human societies; for example, it causes the greenhouse effect, acid rain [3], air pollution, climate change, respiratory diseases, *etc.* [4]. For this reason, denitrogenation and desulphurization of various forms of oil before their entry into the biochemical cycle are very important, and usually many processes including cracking, reforming, isomerization, hydrotreating and hydrocracking are performed during oil refining, by the help of catalysts, to make petroleum a clean fuel for the market, ultimately [2].

In recent years, there have been many studies to refine oil from environmental pollutants. Haji-Shamsaee *et al.* (2019) experimentally performed sulfurous removal of benzothiophene using dynamic electroreduction method. After that, they did it theoretically using Gibbs free energy; the relative responses were derived from the DFT calculations which were consistent with experimental studies. They demonstrated that 23.3%, 38.4% and 48.2% of sulfur content were converted to H_2S after 4 h, 6 h and 8 h, respectively [5].

Misra *et al.* (2017) synthesized a functionalized polymeric adsorbent to selectively absorb quinoline from oil. They removed nitrogen and sulfur compounds at different temperatures, with a yield of 60% and 23%, respectively, and indicated that synthetic adsorbent has a good potential for being used in oil refining technology [6].

In another study, in 2017, quinoline by A.S. Ogunlaja *et al.* was eliminated by two simultaneous oxidation and adsorption processes utilizing vanadium oxide catalyst [7].

Along with the development of science and technology, the attention of researchers has been drawn to the use of the catalysts for removing pollutants from oil. The successful

*Corresponding author. E-mail: r_fazaeli@azad.ac.ir

application of catalytic processes in the elimination of environmental pollutants is related to the catalyst effectiveness with three factors: activity, selectivity, and sustainability [8]. Therefore, advanced modern catalysts in the form of nanocrystalline and nanoporous materials are synthesized by the precise controlling of crystal size, the surface area of the components, the diffusion of components, the structure and pore size [9,10]. In this regard, aluminosilicate compounds including zeolites can be mentioned because of their unique features such as molecular sieves, high vacant spaces, low density, cationic exchange property, electrical conductivity, suitable catalytic and adsorbent properties [11].

Thermont *et al*. investigated various modified zeolites for aqueous solutions absorbing and concluded that zeolite could increase absorption [12,13].

The advanced oxidation process, such as UV/H_2O_2, has been of great interest for the researchers in recent years, because of increasing efficiency and relatively rapid and complete degradation of the pollutant. However, using photocatalysis by semiconductor is more important due to non-toxicity and also its ability to be recycled by straightening or centrifuging compared to the other oxidation methods [14]. Accordingly, among which, oxides or sulfides of the intermediates that are in the term "compound semiconductor" are known to be the most suitable photocatalysts with high resistance to the optical analysis of bandgap energy [15]. These compounds include Fe_2O_3, WO_3, CdS, ZnO, TiO_2 and ZnS semiconductor, which the most active ones are TiO_2 and ZnO.

Several methods have been recently used for enhancing photocatalytic properties for denitrogenation. The Z.Y. Zhang *et al*.'s review on absorption removing of the sulfur aromatic compounds with modified Y zeolites using the various ions exchanging with sodium can be considered as a sample of the zeolite and metal combination [16].

In this research, to remove and degrade quinoline, CuO/MCM-41 nanocomposite was synthesized and characterized by XRD, FESEM, EDS, Mapping, FTIR and BET/BJH techniques. The photodegradation efficiency was evaluated by investigating the operational parameters and process optimization with the help of the statistical methods.

EXPERIMENTAL

Materials

Cetyltrimethylammonium bromide (CTAB), tetraethyl orthosilicate (TEOS), sodium hydroxide (NaOH), copper(II) nitrate trihydrate ($Cu(NO_3)_2.3H_2O$), and quinoline were purchased from Merck Germany. All of the chemicals were used without further purification.

Instruments

X-ray diffraction (XRD). Prepared MCM and nanocomposite were evaluated by XRD (Rigaku, Ultima IV) technique. The measured angle was ranged between 2-70° with a rate of 1°/min.

Field emission scanning electron microscopy (FESEM). The surface morphology of nanoparticle and nanocomposite was performed using FEI NOVANANOSEM 450 electron microscope. Also, the elemental analysis of the nanocomposite was accomplished by an X-ray dispersive microanalyzer (Bruker, X Flash 6110).

Fourier Transmission FTIR Spectroscopy. The vibrational pattern of nanocomposite was performed using an FTIR spectrophotometer (Bruker, Tensor 27 and Equinox 55).

Surface area and pore size distribution. Measuring the surface area of nanoparticle and nanocomposite was performed using the Brunauer-Emmett-Teller (BET) analyzer (BELSORP Mini II), and also the pore size distribution was accomplished using Barret-Joyner-Halenda (BJH) methodology with respect to nitrogen adsorption/desorption isotherm.

UV spectrophotometer. The Duplex UV spectrophotometer (PG instruments, T80+) was used to measure solution absorbance using a 1 cm quartz cell.

Design of experiments (DOE). The Design Expert Software (DX-Version 11.0.3) was used for the experiment design. The RSM procedure was used for test designing. Considering that the materials and their composition for removal had three different levels, in contrastive conditions at each level, they had a different effect on the result. In addition, the area to be tested in the composition of the substances and their response to the highly removed

similarly, unstable and sensitive data were also available in terms of the surface changes of the materials, so the Box-Behnken (BBD) technique was used. In this technique, any sensitivity or mistake in analyzing the material can be described as a stop or block unit. With respect to the number of materials along with a response level, five blocks were introduced for the software to obtain more accurate results [17].

Effect of pH, copper(II) dosage, the density of pollutant and composite mass in pollutant treatment. For designing the test, the effects of the hidden variables on pollutant treatment were performed using previous works, to obtain the selected intervals to the software. After performing the preliminary tests, the confidence interval was determined for each one of the variables, and was also introduced as the confidence interval of each variable to the software.

The pH was ranged from 3-11, the copper(II) content in the composite composition was ranged from 0.01-0.4 M, the density of the effluent was 2 to 32 mg l^{-1}, and the mass of the composite was 0.004-0.12 g. Accordingly, the test version was prepared after entering the declared numbers into the test design software.

Test design table. After the test designing by the software, the experiments were performed according to Table 1.

Preparation of MCM-41. To synthesize MCM-41, at first, we added a mix of deionized water, NaOH 2 M and 2 g CTAB in a balloon. The mixture remained on the stirrer for 30 min at 80 °C. After that, 10 ml of TEOS was gradually added to the contents of the balloon, and then refluxed for 2 h at the same temperature and the resulting mixture was cooled down to the room temperature. Finally, the product was filtered and washed with deionized water and then was placed at 70 °C for 20 h, and finally was placed in a furnace for 1 h at 550 °C with the heating rate of 2^{o}/min [18].

Preparation of CuO/MCM-41 Nanocomposite

CuO/MCM-41 nanocomposite was synthesized through a one-step method. At first, three concentrations of copper(II) nitrate solution (0.01, 0.205, 0.4 M) were prepared. After that, a certain amount of MCM-41 was mixed with 1 ml of each of the mixed solutions of copper nitrate solution, and was placed for 24 h into styrene, respectively. The solution was washed with distilled water and centrifuged, and finally dried at 100 °C and placed in a furnace for calcination at 450 °C [19].

Removal Studies

The quinoline with a maximum absorption wavelength of 313 nm was selected as a pollutant for assessing the adsorption and optical nanocomposite activity. For this purpose, 0.008 g of the different composites was added to the 20 ml quinoline solution at a concentration of 2 mg l^{-1}. To investigate the photocatalytic process, UV light was used in an optical reactor with a mercury lamp, Philips 9W (UV-C).

The pH of suspensions was adjusted to the desired level with NaOH and HCl 1 M. The percentage removal of quinoline %R was defined as a function of time with respect to Eqs. (1) [20]:

$$Efficiency\% = \frac{A_0 - A}{A_0} \times 100$$

where A_0 and A are the quinoline adsorption at t = 0 and t = t, respectively. The effect of nanocomposite concentration on the quinoline removal was investigated by 20 ml quinoline solution with an initial concentration of 2 mg l^{-1} and pH = 7 for 40 min at room temperature. The different amounts of synthetic nanocomposite CuO/MCM-41 (0.004, 0.006, 0.008, 0.01, 0.12 g) were used in order to remove quinoline. In addition, the effects of pH values (3.7,11) and initial concentration of quinoline (2, 17, 32 mg l^{-1}) on quinoline removal by MCM-41 and CuO/MCM-41 were similar to the process of changing the nanocomposite content.

RESULTS AND DISCUSSION

Oxidation Process

From the GC-MASS results, it is generally understood that the photocatalytic reaction occurs and can produce multiple compounds and unstable intermediates that rapidly combined to form multiple products, and they can eventually form gaseous compounds and NH_3, CO_2, H_2O

Table 1. Designing Experiments to Investigate the Effect of Variables on Pollutant Treatment

Run	pH	Cu (M)	Pollutant Conc. (mg l^{-1})	Composite (g)	Efficiency
1	3	0.205	32	0.006	6.21
2	7	0.205	17	0.12	-15.57
3	7	0.205	17	0.12	-11.22
4	3	0.205	2	0.004	-7.87
5	7	0.4	32	0.12	-5.13
6	7	0.4	2	0.01	-69.44
7	3	0.4	17	0.004	4.28
8	11	0.01	17	0.006	-10.42
9	7	0.205	17	0.004	-10.88
10	7	0.01	2	0.006	-46.29
11	7	0.4	32	0.004	-2.96
12	7	0.205	17	0.006	0.16
13	11	0.205	2	0.12	8.49
14	11	0.01	17	0.004	2.79
15	7	0.01	32	0.12	-5.93
16	7	0.01	32	0.008	-6.98
17	11	0.4	17	0.008	5.95
18	3	0.01	17	0.01	-0.17
19	11	0.205	32	0.12	-3.37
20	7	0.205	17	0.12	-9.71
21	7	0.4	2	0.006	-53.70
22	7	0.205	17	0.008	-80.90
23	7	0.01	2	0.004	-41.66
24	3	0.01	17	0.12	14.57
25	11	0.205	2	0.008	-59.43
26	3	0.4	17	0.006	-2.91
27	7	0.205	17	0.008	43.71

Table 1. Continued

28	3	0.205	32	0.12	3.97
29	7	0.205	17	0.004	-0.16
30	7	0.205	17	0.008	5.52
31	7	0.205	17	0.006	-8.20
32	3	0.4	17	0.008	-9.43
33	7	0.01	2	0.008	-37.96
34	11	0.4	17	0.004	-2.23
35	7	0.4	2	0.12	-77.77
36	3	0.205	32	0.004	12.94
37	7	0.4	2	0.004	75.00
38	3	0.01	17	0.004	-14.57
39	7	0.01	32	0.006	10.67
40	7	0.205	17	0.006	22.61
41	3	0.205	2	0.01	44.88
42	7	0.4	2	0.008	-81.48
43	7	0.205	17	0.01	-2.68
44	11	0.205	2	0.006	61.32
45	3	0.205	2	0.12	-3.93
46	7	0.01	2	0.12	-61.11
47	7	0.205	17	0.004	2.17
48	11	0.205	32	0.006	7.89
49	7	0.4	32	0.008	-4.65
50	7	0.4	32	0.006	-7.94
51	3	0.205	32	0.01	7.01
52	11	0.205	32	0.01	84.37
53	7	0.205	17	0.01	-6.19
54	7	0.205	17	0.01	-5.02
55	11	0.205	2	0.01	14.15
56	7	0.205	17	0.008	6.19
57	11	0.4	17	0.006	3.16

Table 1. Continued

58	7	0.01	2	0.01	-15.74
59	11	0.4	17	0.12	0.00
60	7	0.205	17	0.004	-11.05
61	11	0.205	2	0.004	-72.64
62	11	0.01	17	0.12	0.37
63	3	0.4	17	0.12	11.83
64	11	0.01	17	0.008	5.77
65	11	0.205	32	0.008	12.17
66	3	0.4	17	0.01	17.49
67	7	0.205	17	0.008	5.36
68	11	0.01	17	0.01	4.09
69	3	0.01	17	0.006	9.94
70	7	0.205	17	0.01	-8.54
71	7	0.01	32	0.01	-5.21
72	7	0.01	32	0.004	-2.08
73	7	0.205	17	0.006	-16.91
74	7	0.205	17	0.01	11.05
75	3	0.205	2	0.008	-77.16
76	7	0.205	17	0.004	-7.03
77	7	0.205	17	0.12	14.57
78	7	0.4	32	0.01	2.80
79	7	0.205	17	0.006	16.08
80	11	0.205	32	0.004	7.15
81	3	0.205	2	0.006	-55.90
82	11	0.4	17	0.01	-15.27
83	7	0.205	17	0.12	11.72
84	3	0.01	17	0.008	-0.51
85	3	0.205	32	0.008	-3.83

molecules.

The chromatogram test number 6 (from Table 1) is shown in Fig. 2. Peak 13.077 is related to quinoline. There are several other peak clusters that classified into three categories: one is a cluster of molecules that cannot be linked to a reaction mixture, which is generally a mixture of internal standard GC-MASS molecules and previous contamination of the device column (device noise). The other one is a group of molecules produced by the quinoline oxidation and degradation. The third peaks can also be associated with the separation and reactivity of the MCM catalyst containing the silane compounds. The first point is that the type of catalytic reaction occurred is photocatalytic degradation type such that the destruction and degradation of the quinoline structure occurred in the presence of light. The major products of the photocatalytic reaction include CO_2, NO_3^- and NH_4^+; however, it also had unreacted quinoline and organic compounds and intermediates that were caused by quinoline decomposition.

The residual quinoline concentration in the reaction mixture can be calculated with respect to the concentration of the internal standard substance and the surface area under their peaks. Of course, we must have a standard internal concentration. By dividing the peak area of quinoline by the peak area of the internal standard, a ratio can be obtained that can be compared for different tests.

The molecular structures arising from the breakdown of the quinoline is shown next to the spectrum. Here are some mechanisms for some of these molecules formation:

And finally, similar mechanisms can be found for the rest of the compounds. The chromatogram test 37 is also displayed in Fig. 7.

Peak 13.077 is related to quinoline. As in the spectrum of Test 6, we have almost identical structures in this spectrum. The molecular structure from the breakdown of quinoline is shown next to the spectrum. The mechanism 5 is shown in Fig. 8 for some of these molecules' formation:

Table 2 compares the results of these two tests. Given the area of quinoline peaks and the internal standard, a ratio can be obtained, which is lower than the residual quinoline concentration in the reaction, provided that the internal standard concentration in both GC-MASS spectra is similar. This ratio determines the residual quinoline concentration if multiplied by the standard internal concentration used. According to Table 2, it appears that the higher the catalyst content, the more quinoline removal occurrs.

Figure 9 is associated with the formation of two substances in the spectrum. Most compounds were earlier described as their mechanism.

With respect to the GC-MASS data of Tests 6 and 37, it can be said that the negative efficiency of test 6 is not an indicator of zero or negative quinoline concentration. In fact, it appears that most of the 69% of quinoline is lost and some quinoline is still present. It is in the spectrum and we can observe compounds from the analysis. In a situation that the efficiency is zero, no quinoline in the spectrum should be observed. At this stage, the observed absorption peak in UV spectroscopy is the result of residual quinoline (up to about 31%) and the side effects of the decomposition shown, and the sum of these absorptions negates the resulting percentage. Accordingly, this result is in agreement with credible scientific sources indicating that the absorption peak of quinoline derivatives is in the quinoline self-absorption region [22].

Design of experiments (DOE). According to Table 1, the largest amount of pollutant treatment belonged to the test number 52, which indicated that it was increased by raising the amount of pH to the alkaline soluble medium, along with increasing the amount of composite in gram unit; the pollutant treatment was also raised. According to the Test number 65, and, in comparison with experiment number 52, all parameters were similar, only the composite value on test 65 was less, so it can be concluded that reducing the amount of composite will reduce the amount of removal.

From Table 1, in the first view, it can be concluded that all the variables in the experiment require alignment and balance to optimize the removal process. This replication and balance will be based on the output of the statistical results, as well as the optimal version with the help of the BBD method and also the created blocks.

Statistical analysis. According to Table 3, the validity of the test in the RSM model was less than 0.05 (0.0462), there is a significant difference between the variables effect on pollutant treatment. Therefore, it can be concluded that pH, copper, pollutant density and the amount of composite have significant effects on pollutant treatment. Also, due to

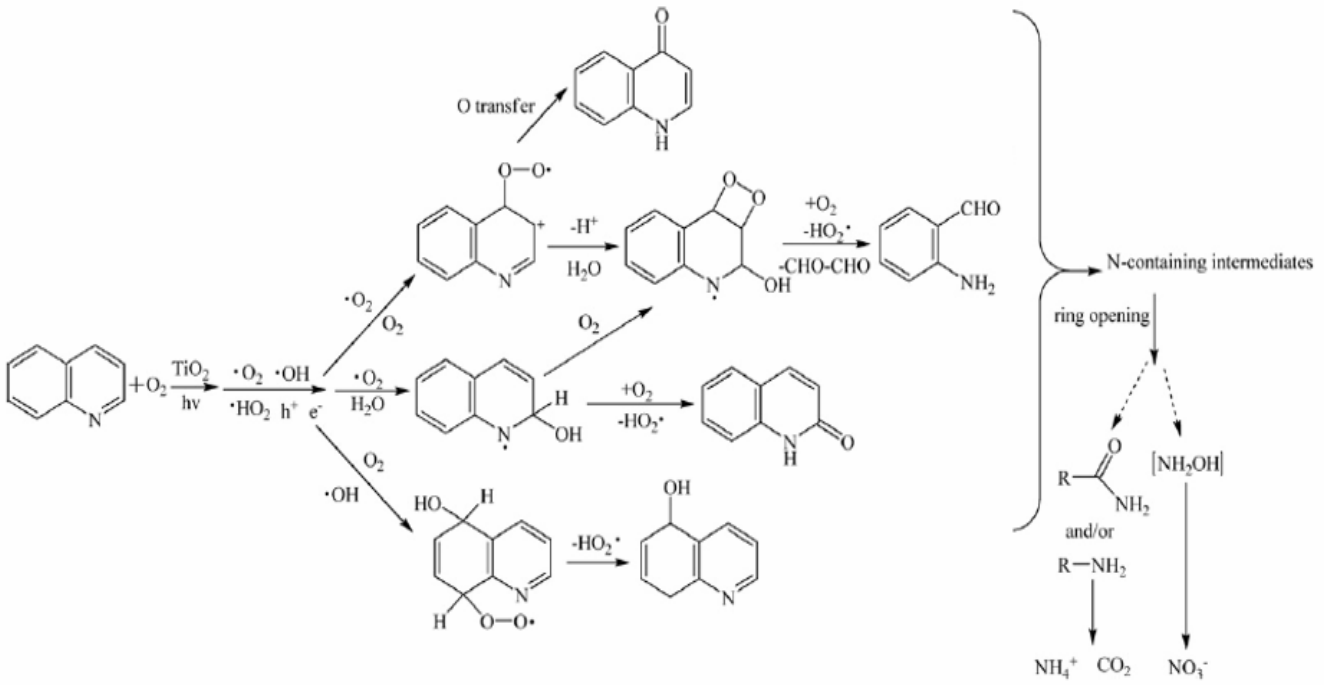

Fig. 1. Postulated pathways of quinoline photodegradation over TiO_2 nanoparticles under UV irradiation [21].

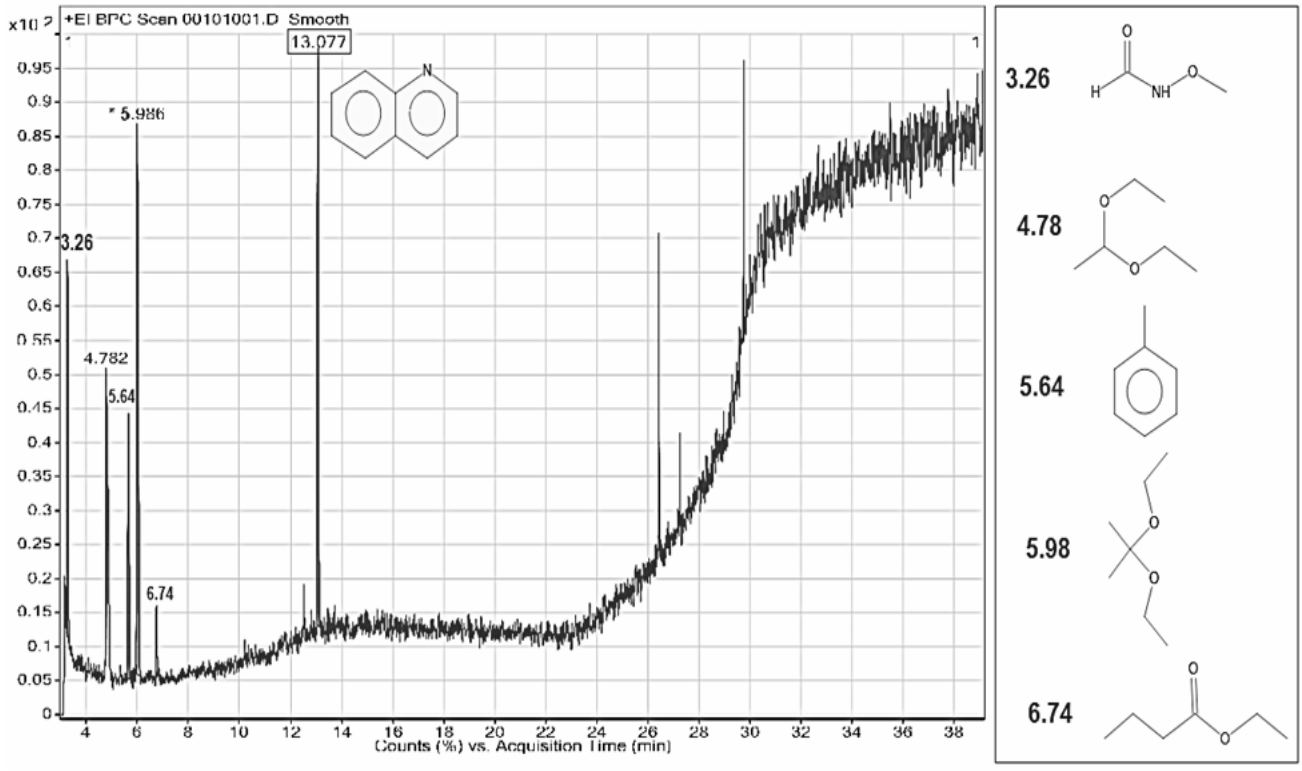

Fig. 2. Chromatogram for Test Number 6.

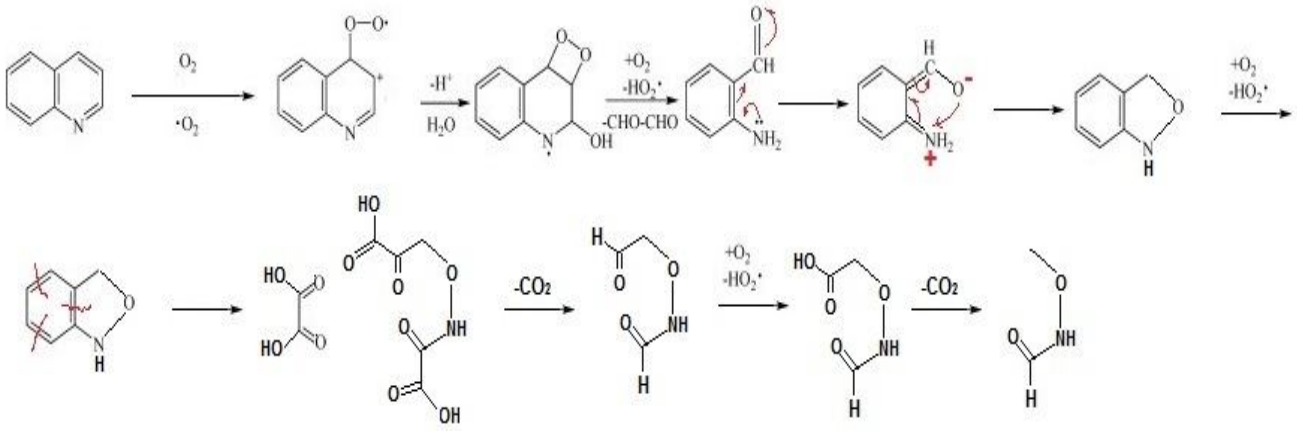

Fig. 3. Mechanism 1 is related to peak 3.26.

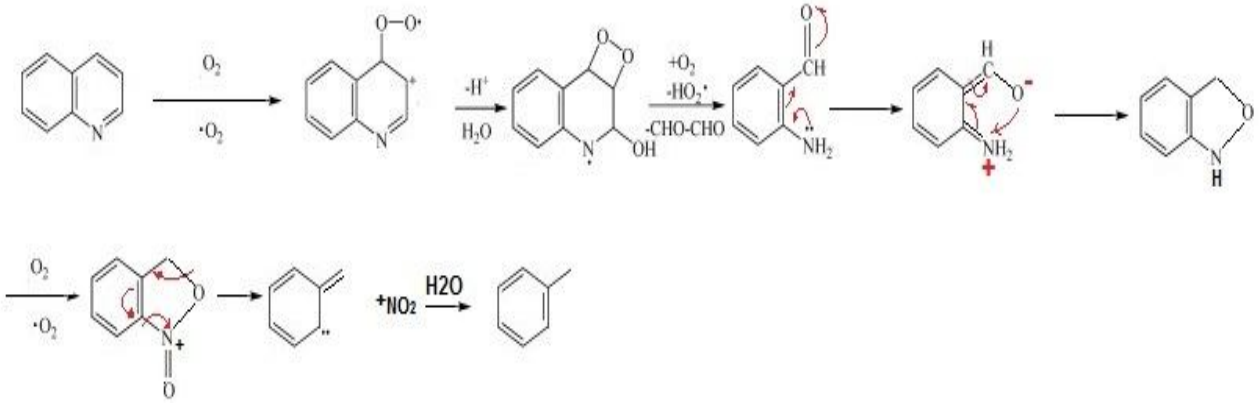

Fig. 4. Mechanism 2 is related to the 5.64 peak.

the fact that the F test statistic in pollutant density has increased the model's value, it has greater effect on pollutant treatment. It is notable to state that the composite variable statistic is more than the pH and copper variables, indicating that in comparison with each other, the amount of composite variable volume has the greatest effect on their effluent treatment, too [23,24]. Moreover, the mathematical model of the experimental design is as follows:

Removal (composite 0.004) = -50.6076 + 3.93245 × [pH] + 172 × [Cu] + 0.873672 × [Pollutant Density] + -7.65894 × [pH] × [Cu] + 0.245747 × [pH] × [Pollutant Density] + -10.047 × [Cu] × [Pollutant Density] + -0.600418 × $[pH]^2$ +330.496 × [Cu]2 + -0.000462975 × $[Pollutant\ Density]^2$

(2)

Removal (composite 0.006) = -72.5379 + -1.83266 × [pH] + 113.255 × [Cu] + 6.1669 × [Pollutant Density] + 8.4803 × [pH] × [Cu] + -0.481458 × [pH] × [Pollutant Density] + -0.958307 × [Cu] × [Pollutant Density] + 0.824854 × $[pH]^2$ + -420.835 × $[Cu]^2$ + -0.0491674 × $[Pollutant\ Density]^2$

(3)

Removal (composite 0.008) = -57.7471 + -1.00656 × [pH] + -139.32 × [Cu] + 5.98196 × [Pollutant Density] + 2.91846 × [pH] × [Cu] + -0.00720042 × [pH] × [Pollutant Density] + 3.91846 × [Cu] × [Pollutant Density] + 0.1616 × $[pH]^2$ + 49.4495 × $[Cu]^2$ + -0.136136 × $[Pollutant\ Density]^2$

(4)

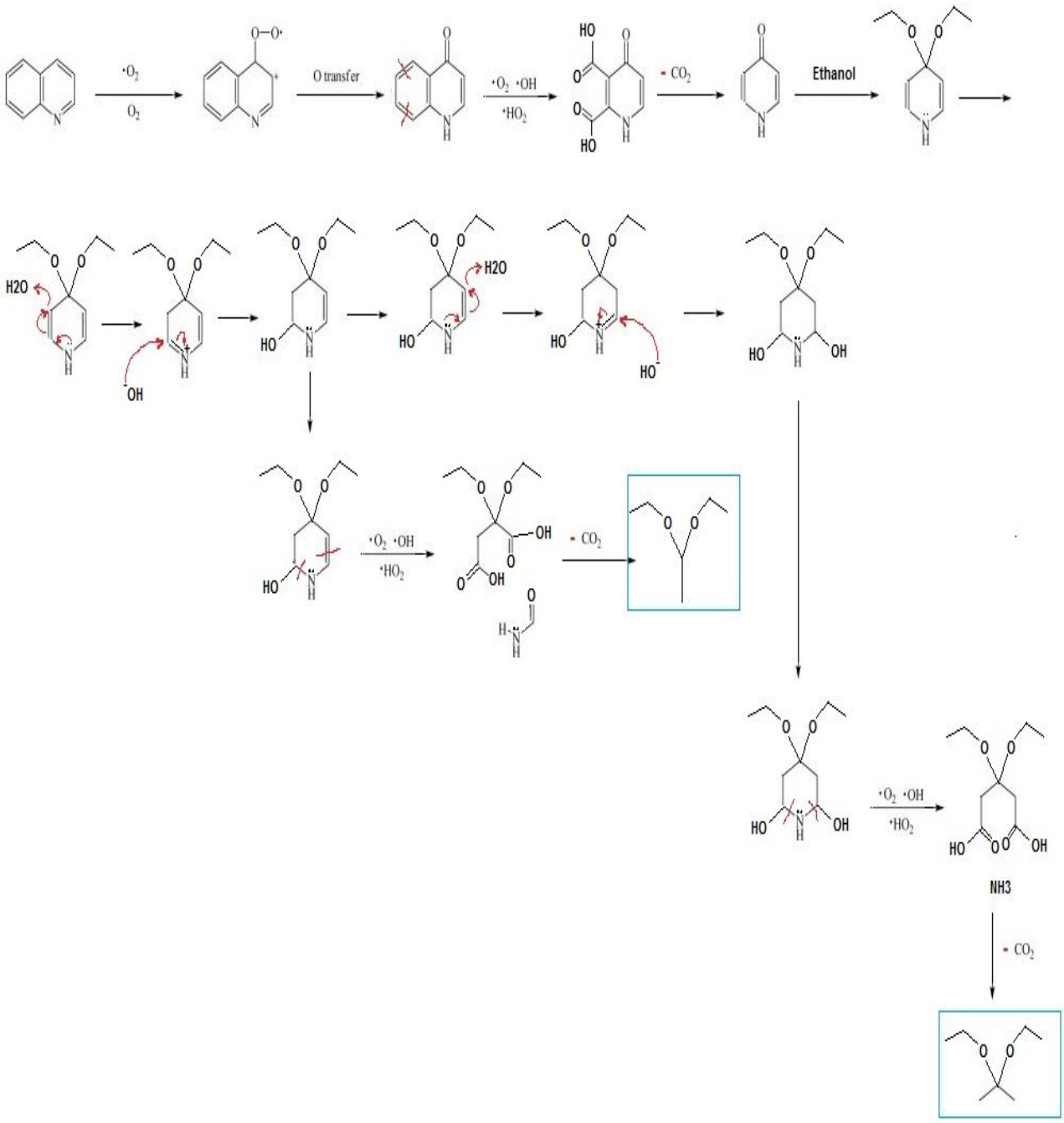

Fig. 5. Mechanism 3.

Removal (composite 0.01) =115.368 + -32.3588 × [pH] + 263.25 × [Cu] + -4.51753 × [Pollutant Density] + -11.8699 × [pH] × [Cu] + 0.450384 × [pH] × [Pollutant Density] + 5.27602 × [Cu] × [Pollutant Density] + 1.97873 × $[pH]^2$ + -732.252 × Cu^2 + 0.03655 × $[Pollutant\ Density]^2$ (5)

Removal (composite 0.12) =13.9066 + -20.2007 × [pH] + 119.081 × [Cu] + 4.38973 × [Pollutant Density] + 0.760254 × [pH] × [Cu] + -0.0824006 × [pH] ×Pollutant Density + 1.4931 × [Cu] × [Pollutant Density] + 1.48504 × $[pH]^2$ + -395.008 × $[Cu]^2$ + -0.0907883 × $[Pollutant\ Density]^2$ (6)

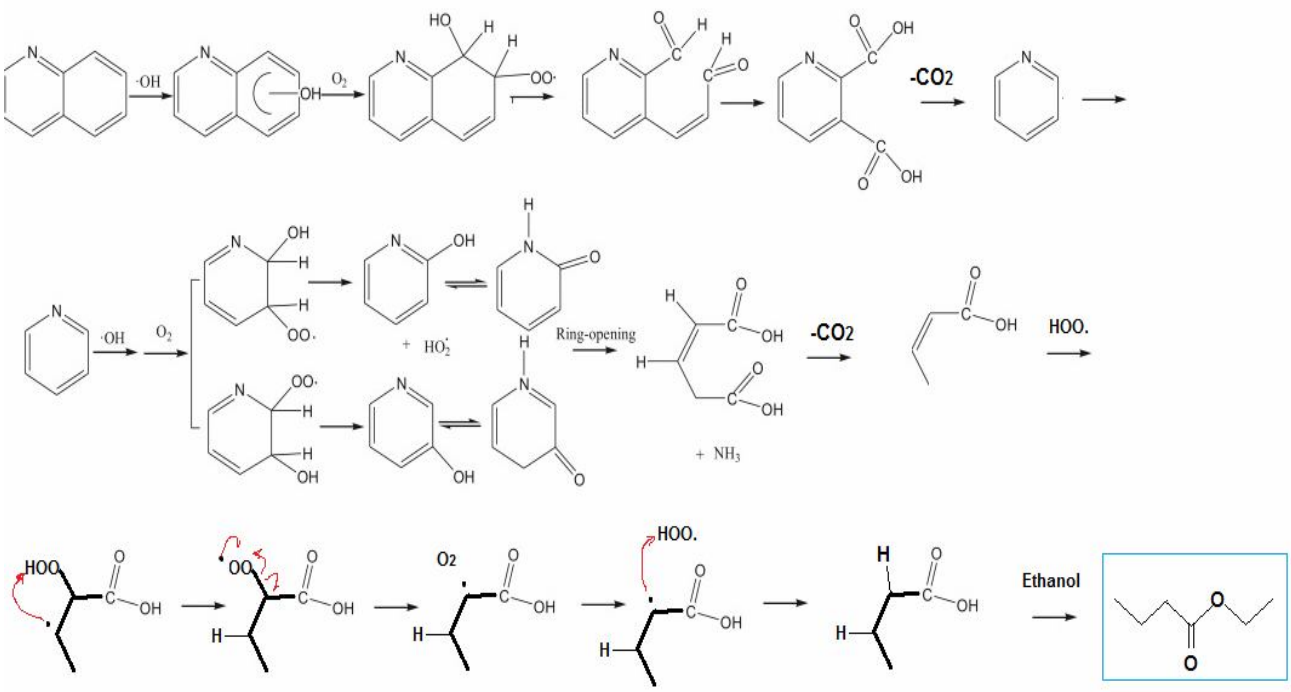

Fig. 6. Mechanism 4.

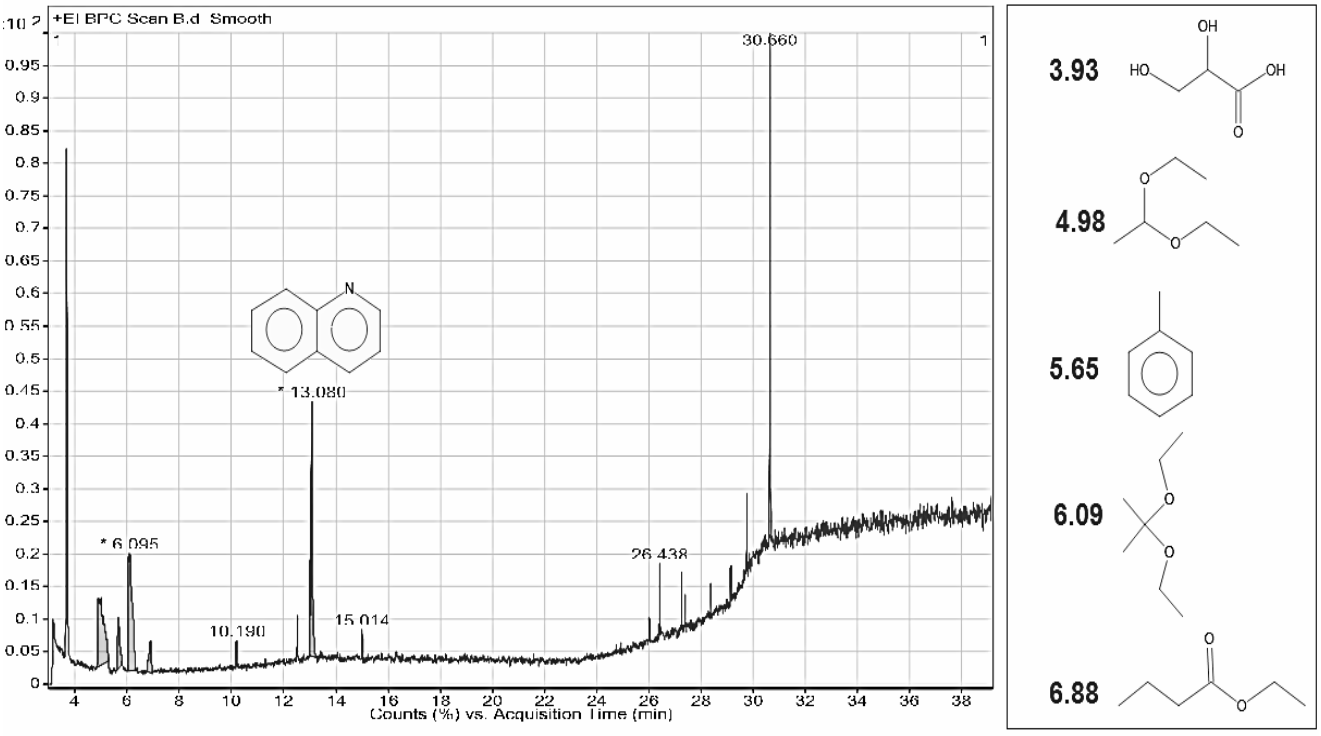

Fig. 7. Chromatograph diagram of test number 37.

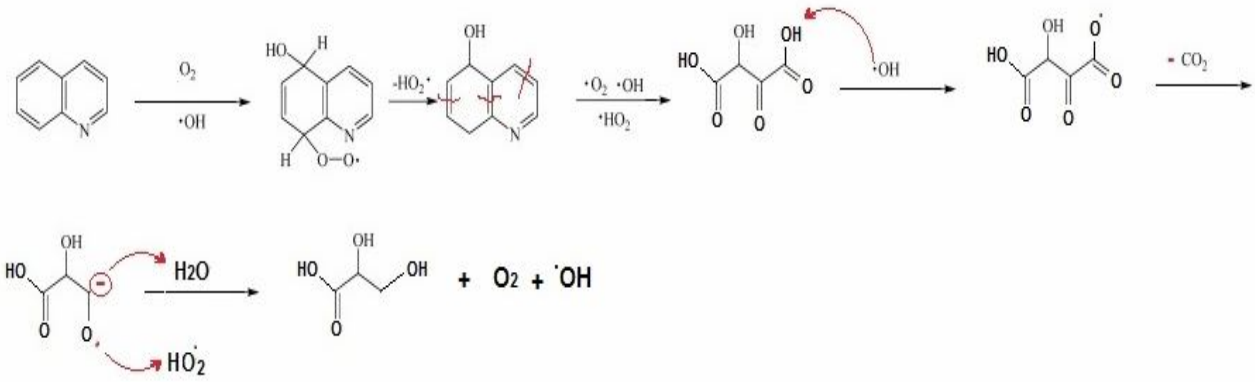

Fig. 8. Mechanism 5.

Table 2. Comparison between 2 Tests

TEST	Efficiency (%)	Composite g	Area 1 (quinolone 13.07)	Area 2 (IS 26.43)	Ratio A1/A2
6	-69.44	0.01	17162	6435	2.66
37	75	0.004	45253	4259	10.62

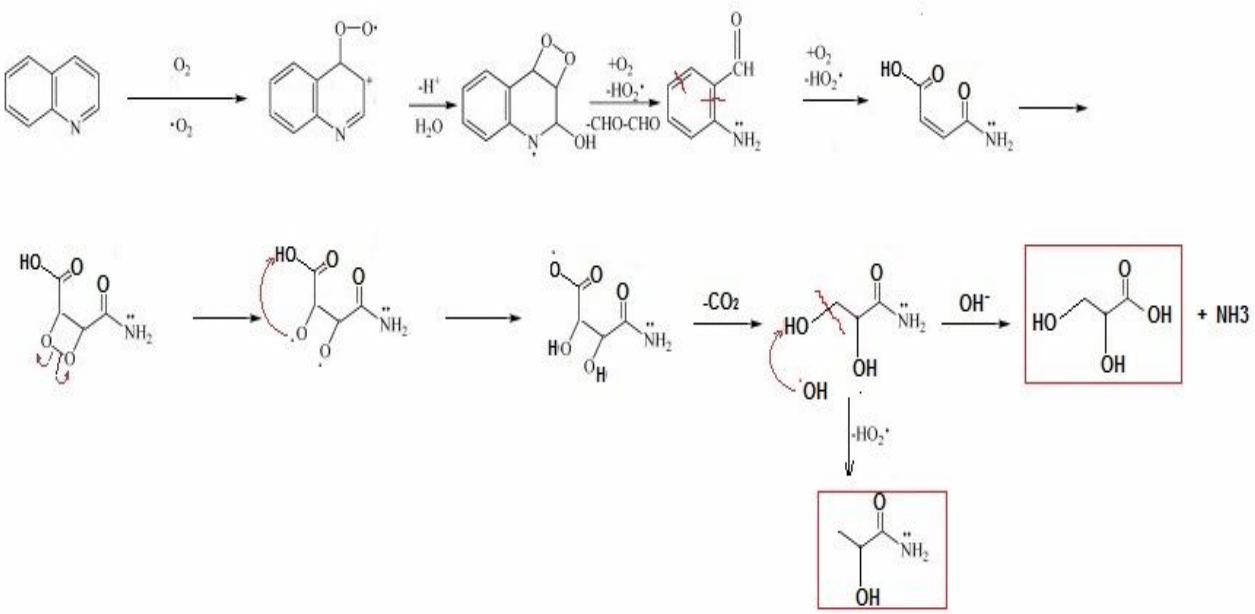

Fig. 9. Mechanism 6.

Table 3. ANOVA Analysis of the Pollutant Treatment

ANOVA response surface methodology with cubic model						
Source	Sum of squares	Df	Mean Square	F-value	P-value	
Model	54639.92	49	1115.10	1.73	0.0462	Significant
A-pH	237.59	1	237.59	0.3680	0.5480	
B-Cu	3.57	1	3.57	0.0055	0.9411	
C-Pollutant density	11068.73	1	11068.73	17.15	0.0002	
D-composite	3492.65	4	873.16	1.35	0.2702	
AB	26.44	1	26.44	0.0409	0.8408	
AC	45.05	1	45.05	0.0698	0.7932	
AD	2055.73	4	513.93	0.7961	0.5358	
BC	0.6909	1	0.6909	0.0011	0.9741	
BD	2813.88	4	703.47	1.09	0.3767	
CD	2527.04	4	631.76	0.9786	0.4317	
A^2	3195.10	1	3195.10	4.95	0.0326	
B^2	1661.50	1	1661.50	2.57	0.1176	
C^2	2455.68	1	2455.68	3.80	0.0592	
ABD	656.35	4	164.09	0.2542	0.9052	
ACD	7182.03	4	1795.51	2.78	0.0417	
BCD	5039.60	4	1259.90	1.95	0.1236	
A^2D	4552.51	4	1138.13	1.76	0.1584	
B^2D	4310.82	4	1077.70	1.67	0.1791	
C^2D	4051.85	4	1012.96	1.57	0.2042	
Residual	22595.06	35	645.57			
Lack of fit	11853.86	15	790.26	1.47	0.0207	Significant
Pure error	10741.20	20	537.06			
Cor total	77234.98	84				

The normal probability chart indicates how variables follow a normal distribution. Even with normal data, there are still some moderate distributions. Curved patterns like the "S-shape" that are recognizable with a single look demonstrate that by performing a transfer function on the dependent variable or the model response, better analysis

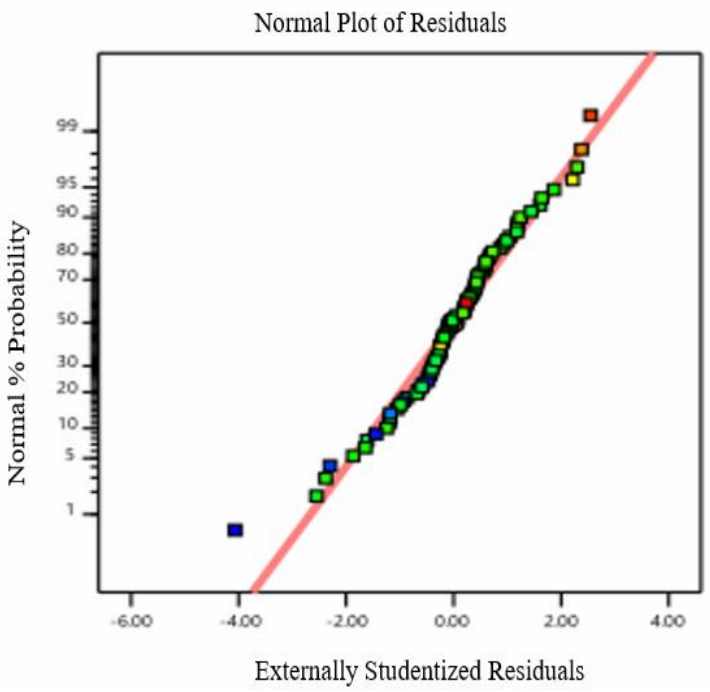

Fig. 10. Scattering diagram of the normal distribution of the variables' response.

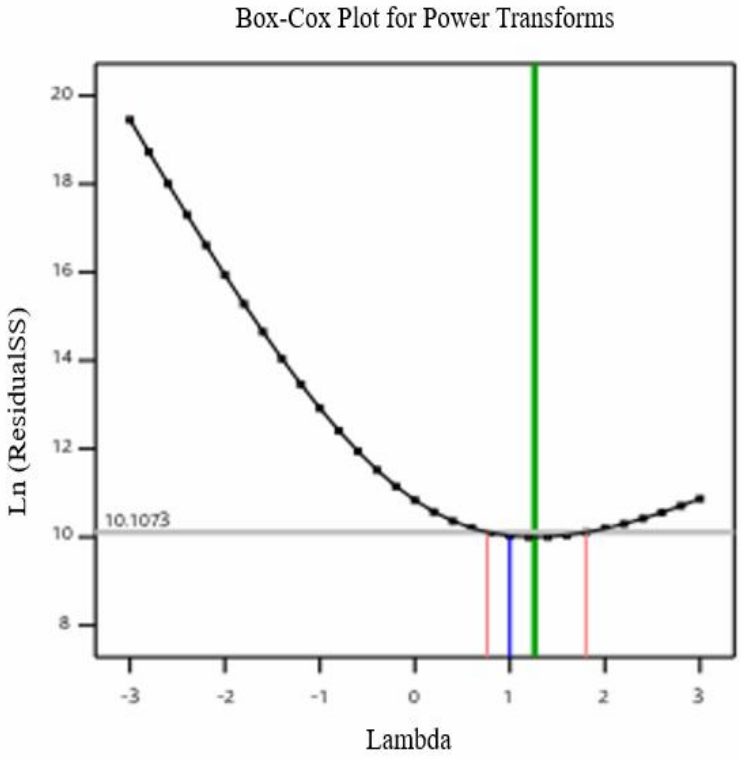

Fig. 11. Box -Cox diagnosis test for pollutant treatment.

will be obtained.

With respect to Fig. 10, the distribution of normal dispersion of variables is shown linearly. Since the distribution of variables is almost symmetrical, and also for each variable in the low level of symmetry, a variable is located at the high level of its symmetry, therefore, it can be stated that the statistical society of the pollutant treatment data has a normal state. The normal state of the data indicates the correct results and the user accuracy.

Box-Cox is a tool to help identifying the most appropriate transfer function for applying the response. The lowest point in the box indicates the best value of lambda, which is the least sum of squares remained in the transformed model. When the ratio of the maximum to the minimum response value is more than three, there will be more ability for improving the model by the use of the power function. With respect to Fig. 11, in which the difference between minimum and maximum is 3, a higher potential improvement for the test model cannot be considered. According to Fig. 11, Lambda simulates the creation of a mathematical computational link between variables in current and also the actual value was specified. The best point for simulation and getting optimal of experiments is introduced in 1.12.

The behavior of variables on removal treatment. Using the analysis of the three-dimensional diagrams obtained from the experiments, the effect of the variables and their behavior in the experiment can be observed.

In Fig. 12, along with the increase of copper molar content, the pollutant treatment process has also elevated. This process simultaneously depends on the pH value. As the amount moves toward the alkaline soluble medium, the effect on the pollutant treatment is getting evident. The important point in this diagram is the existence of a red area of the model for the purpose of predicting the status of the pollutant treatment in the conditions stated by the software. Regarding this software, if the alkaline soluble medium can be raised more, the most pollutant treatment will occur in the case of copper molar nearly one. The overall diagram indicates that the materials at different test levels have different interactions.

In Fig. 13, by increasing the amount of pollution, the pollutant treatment plant will be affected, but the important point in this section is the correlation between the pH and density variables. As it was specified in the green section of the chart, along with the pH increase, in all places of the amount of pollution density variable, the removal treatment can be observed.

In Fig. 14, the behavior of two variables that were effective in the experiments is clear. The variability of the contamination density has the greatest impact on pollutant treatment according to Table 3, and this effect can be obtained simultaneously by increasing the amount of copper molar in the composite as shown in Fig. 14. In other words, the amount of copper as an interfering variable in composite composition at that time of reaching the density of contamination can have a direct and significant effect on pollutant treatment increasing.

XRD Analysis

The X-ray diffraction analysis is a suitable means of proving the crystallinity and structure of the MCM-41. The main Miller indices and the MCM-41 characteristic shown in Fig. 15 with the star sign, were (100), (110) and (200), from left to right, respectively [25,26]. In the primary structure, Brag reflections were observed in the low area $2\theta = 2.5\text{-}10°$, which was frequently used to identify the MCM-41 structure (Reference code: 00-049-1711). The crystal size of the samples was obtained using Scherrer Eq. (7),

In Fig. 14, the behavior of two variables that were effective in the experiments is clear. The variability of the contamination density has the greatest impact on pollutant treatment according to Table 3, and this effect can be obtained simultaneously by increasing the amount of copper molar in the composite as shown in Fig. 14. In other words, the amount of copper as an interfering variable in composite composition at that time of reaching the density of contamination can have a direct and significant effect on pollutant treatment increasing.

XRD Analysis

The X-ray diffraction analysis is a suitable means of proving the crystallinity and structure of the MCM-41. The main Miller indices and the MCM-41 characteristic shown in Fig. 15 with the star sign, were (100), (110) and (200), from left to right, respectively [25,26]. In the primary structure, Brag reflections were observed in the low area

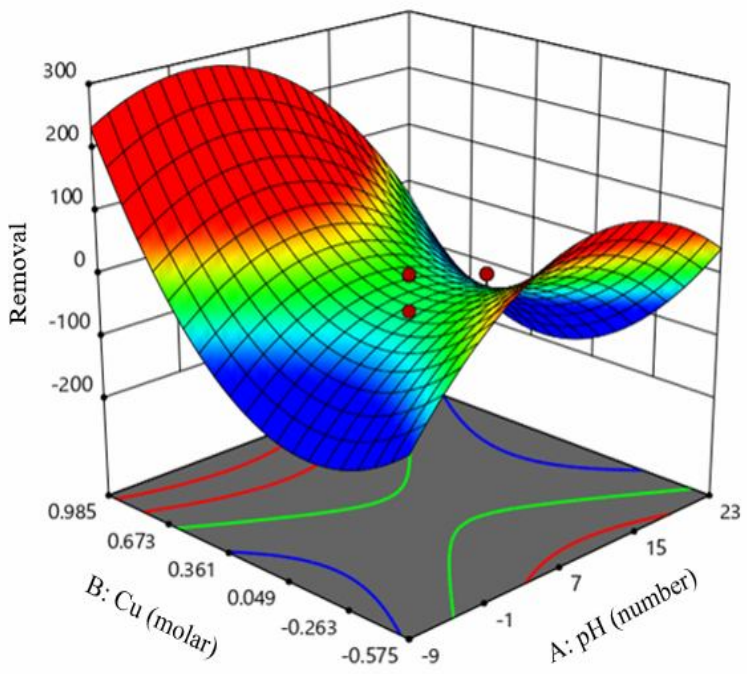

Fig. 12. Three-dimensional diagram of the relationships and influences of pH and copper on pollutant treatment.

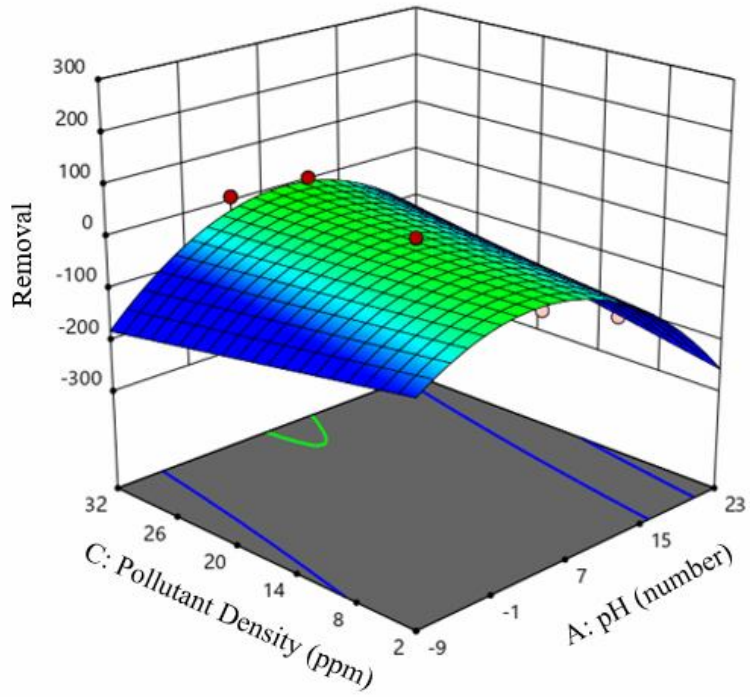

Fig. 13. Three-dimensional diagram of relationships and influences of pH variable and density of pollution on pollutant treatment.

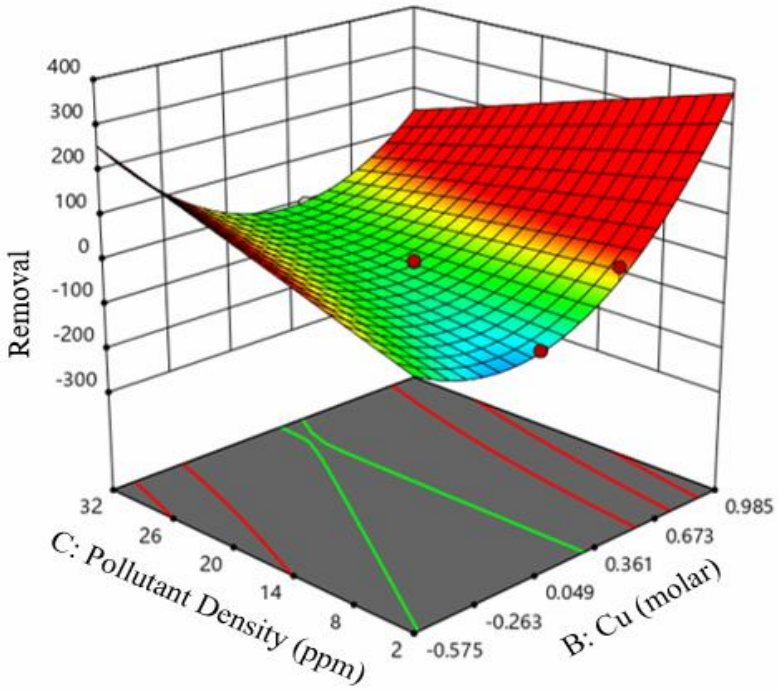

Fig. 14. The three-dimensional diagram of the relationships and effects of copper variable and the pollution density on pollutant treatment.

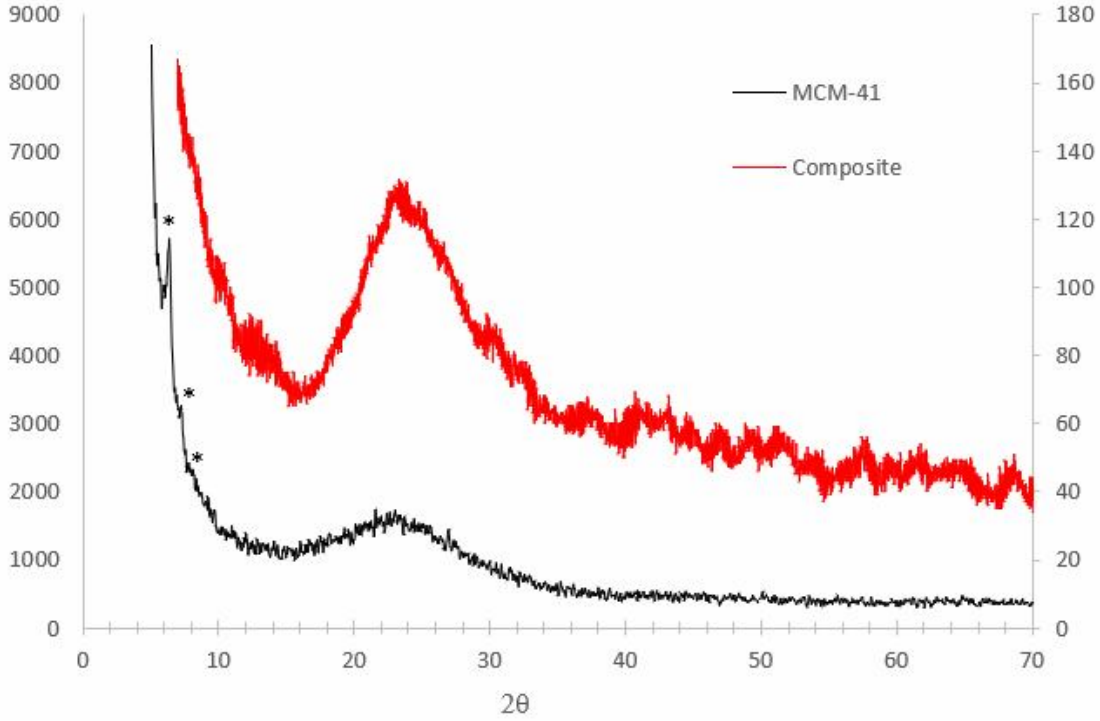

Fig. 15. The XRD Patterns.

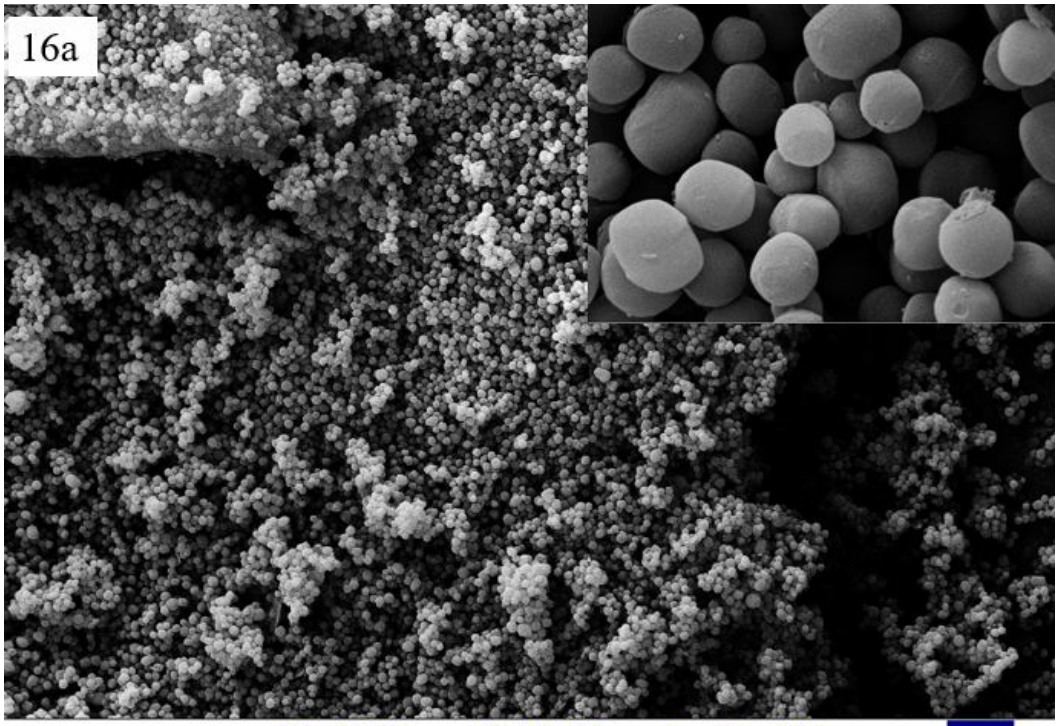

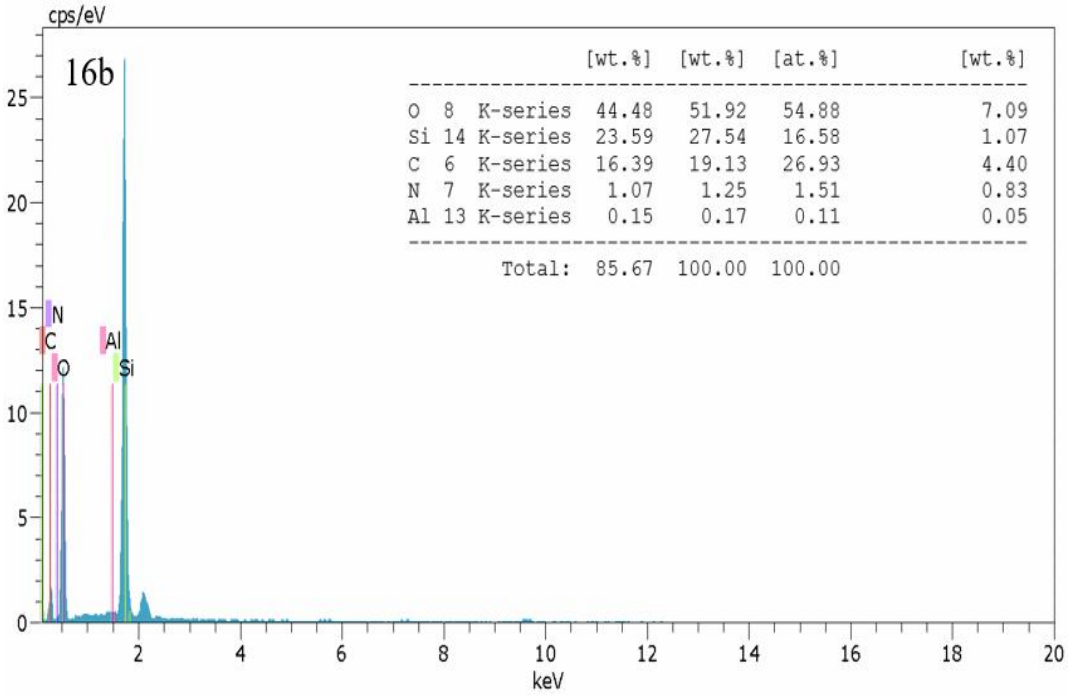

Fig. 16. a) FESEM and b) EDX of MCM-41.

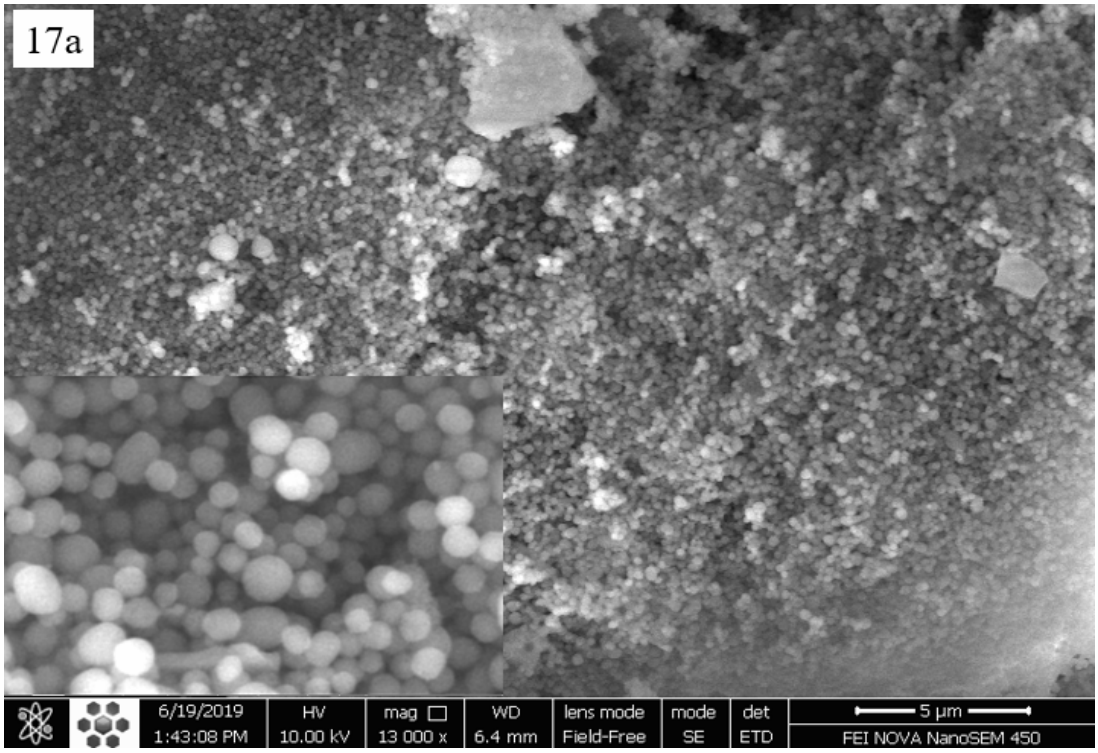

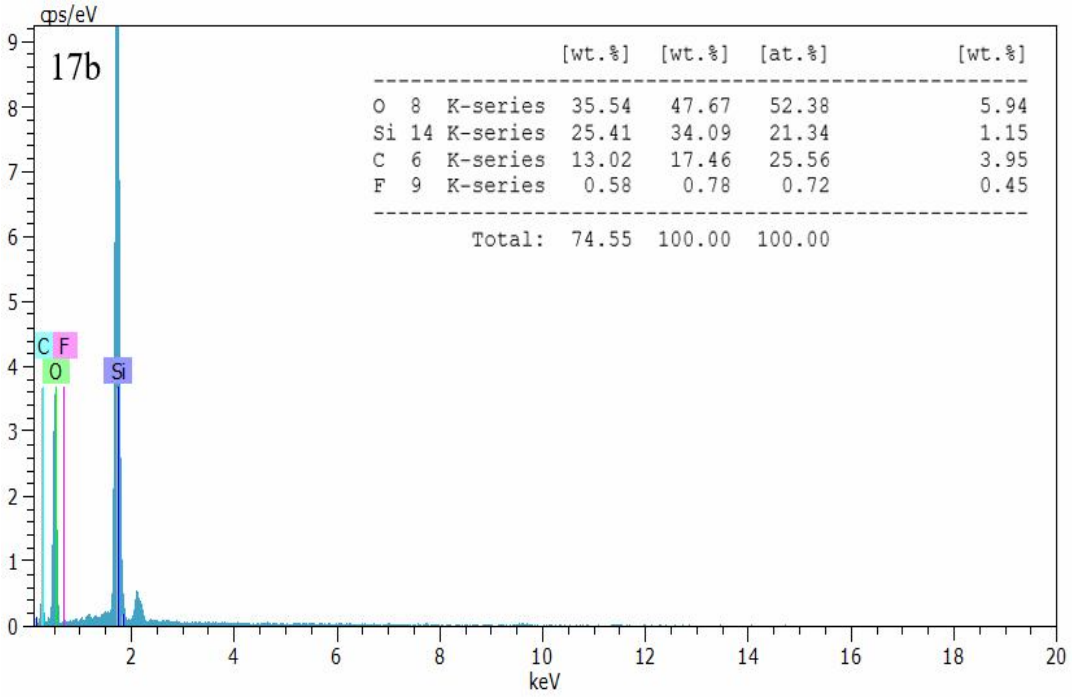

Fig. 17. a) FESEM and b) EDX of composite.

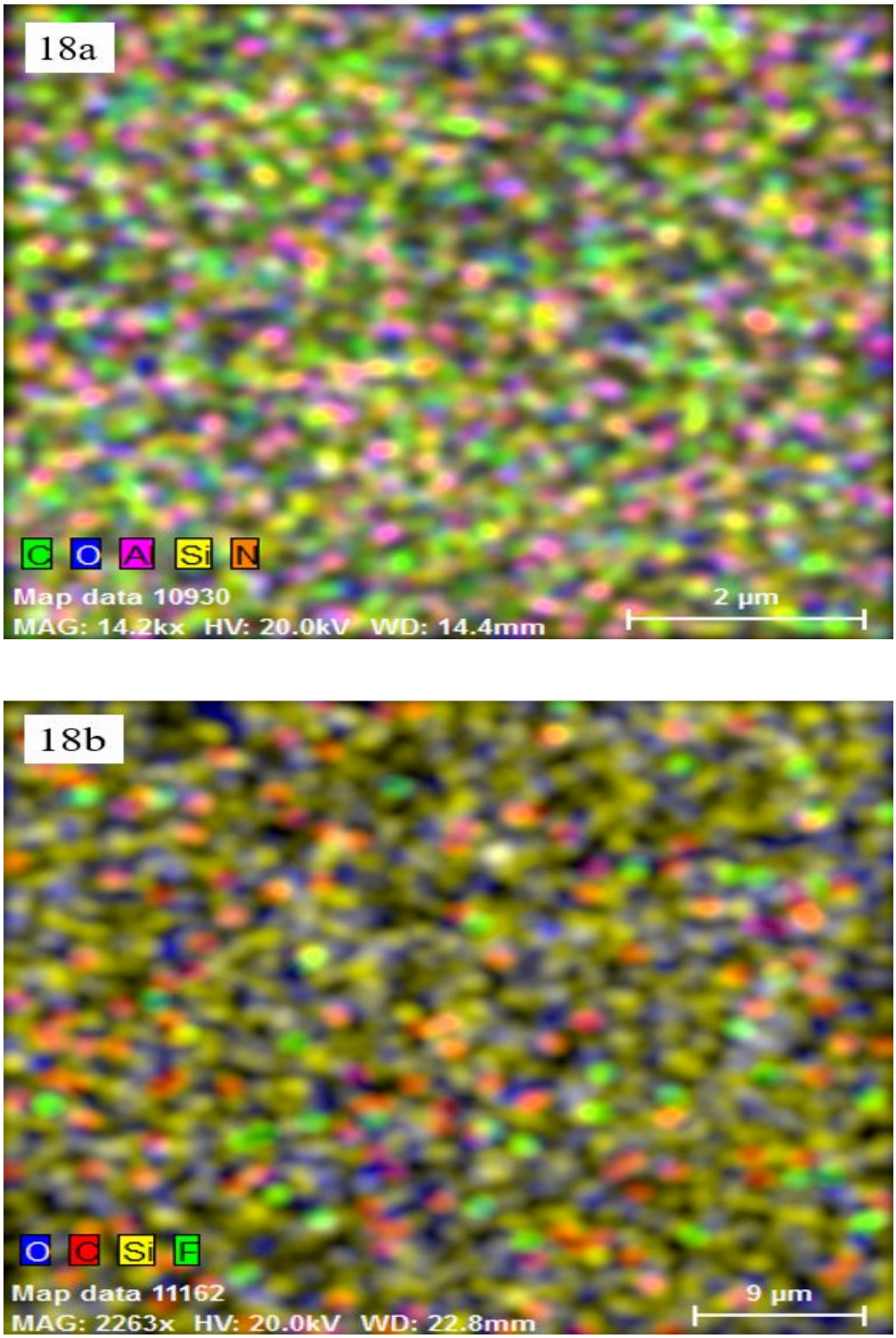

Fig. 18. Mapping patterns of a) MCM-41 and b) composite.

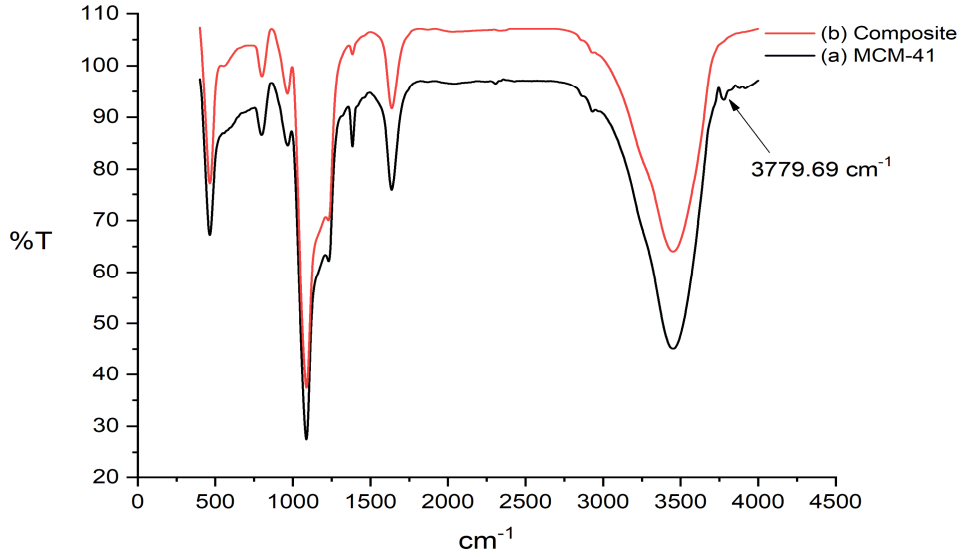

Fig. 19. FTIR patterns of a) MCM-41 and b) composite.

Table 4. Summary of BET and BJH Plot

	BET Plot		BJH Plot (Adsorption branch)	
	Total pore volume (p/p0 = 0.990) ($cm^3\ g^{-1}$)	Mean pore diameter (nm)	$r_{p,peak}$ (Area) (nm)	a_p ($m^2\ g^{-1}$)
MCM-41	0.900200	3.083	2.435	1603.818
Composite	0.051736	13.878	1.210	4.0437

2θ = 2.5-10°, which was frequently used to identify the MCM-41 structure (Reference code: 00-049-1711). The crystal size of the samples was obtained using Scherrer Eq. (7),

$$D = k\lambda/\beta\cos\theta \quad (7)$$

where D is the mean of the crystalline dimension, k is the crystal constant and is 0.89, θ is the Bragg angle, λ is the wavelength of X and β = FWHM, (the acronym is Full Width at Half Maximum) with radian unit for XRD desired peaks.

With respect to the Debye Scherrer model, the crystallite size was estimated to be between 3.77231 and 16.92718, and the mean particle crystallinity was 9.41nm [27].

Although the overall structure of MCM-41 did not change during the synthesis and calcination process, the peak intensity decreased at 2θ = 23 and the characteristic peak of MCM-41 was disappeared at 2θ = 2.5-10°, as a result of the coating of the MCM-41 surface by the amorphous or crystalline particles of CuO. As can be observed from the results, the peak intensity for the CuO/MCM-41 sample decreased. These results are consistent with studies by other researchers, probably due to lower thermal and chemical stability [25,28-30].

After calcining the composite, no peaks in association with $Cu_2(OH)_3.NO_3$ formation was observed in the MCM-41 channels, and rather, peaks at 2θ = 22.9, 27.64, 35.069,

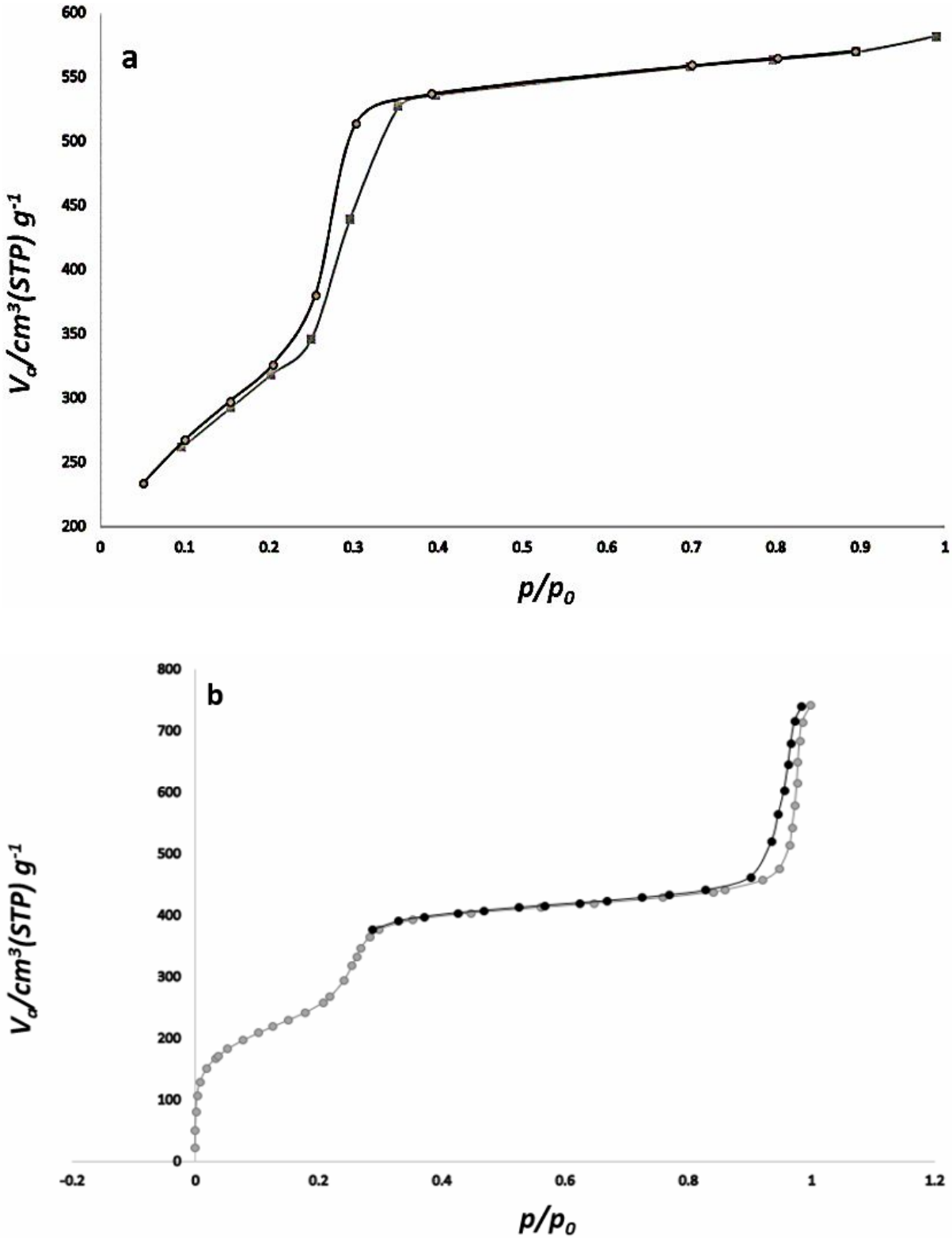

Fig. 20. Adsorption/desorption isotherms of a) MCM-41 and b) composite.

Table 5. Isotherms, Error Minimization and Correlation Maximization

No.	Model	Equation	Correlation coefficient	Error function value
1	Khan	$q_e = \frac{q_{SK}.b_K.C_e}{(1+b_K.C_e)^{a_K}}$	0.98736	28.274%
2	Koble-Corrigan	$q_e = \frac{A.C_e^n}{1+B.C_e^n}$	0.99147	29.02%

Table 6. Optimal Version

pH	Cu	Pollutant density	Composite	Removal	Desirability	Desirability (w/o Intervals)
11.000	0.206	32.000	0.01	84.375	0.802	0.981

47.008 corresponding to CuO formation on MCM-41 were observed (JCPDS # 05-0661) [27]. The presence of weak peaks for CuO can be related to the low amount of CuO in the composite.

FESEM, EDX and Mapping Analyses

The morphology of the samples was investigated using FESEM. Figures 16a and 17a show the FESEM images of MCM-41 and composite particles, respectively. It is clear from the images that the MCM-41 particles are agglomerated. Figures 16a and 16b show the FESEM and EDS of MCM-41 particles before each reaction. Since the obtained FESEM magnification is low in EDS analysis conditions, the FESEM images are displayed at higher magnification in Figs. 16a and 17a, respectively. The formation of copper(II) oxide was confirmed in these analyzes. The chemical purity of the samples was investigated by applying EDS analysis. Figure 16b is the peaks of Si, N, Al and O. Accordingly, these peaks are related to MCM-41. Figure 17b shows the EDS spectrum of the nanocomposite after calcination. This analysis, which is consistent with the XRD spectra, indicates that copper oxides are present in MCM-41. According to EDS analysis, the molar ratio of copper to oxygen is 1:1, which is in agreement with the XRD analysis. The lack of copper in this model is as a result of its very low loading. The distribution of different atoms on the surface of the crystal lattice is also shown in the form of mapping patterns in Fig. 18.

FTIR Analysis

The FTIR spectra of the raw MCM-41 and the CuO/MCM-41 samples are shown in Fig. 19. Also, the metal encapsulated in MCM-41 and the crystallized MCM-41 were confirmed using FTIR peaks. The FTIR spectrum has a strong absorption band to detect MCM-41. The wide peak was in the range of 3400-3700 cm^{-1}, due to the hydroxyl groups (Fig. 19a). The vibrations within the 1300-4600 1700-2700 cm^{-1} peak network indicated no broad transition or discontinuity in the main MCM-41 absorption peak, due to the presence of metal complexes or metal oxide nanoparticles. Accordingly, it was caused by the low concentration of metal loaded on MCM-41. Most MCM-41 peaks are broad and strong. Therefore, the matrix within the spatial structure of MCM-41 was expected to be associated with the peak of MCM-41. This quantity is ranged from1300-1630 cm^{-1}. If the sample absorption peak is present, it can be easily detected and not otherwise detected [31]. In regard with the FTIR spectrum of the sample containing copper oxide nanoparticles and comparing it with the raw MCM-41, it can be observed from the spectrum that was appeared in the core MCM-41 spectrum (1086 cm^{-1}) in the higher region. This peak was shifted to

Table 7. Parameters Value and Greek Letters [33]

A	Koble-Corrigan constant ($l\ nmg^{-1}\ ng^{-1}$)
B	Koble-Corrigan constant ($l\ mg^{-1}$)n
B_S	Sips model exponent
B_{RP}	Radke-Prausnitz models exponents
C	Fritz-Schlunder(IV) constant
C_e	Equilibrium concentration of adsorbate ($mg\ l^{-1}$)
C_S	adsorbate monolayer saturation concentration ($mg\ l^{-1}$)
D	Fritz-Schlunder(IV) constant
E_A	Characteristic energy of adsorption
F, H	Jossens constant
K_E	Elovich equilibrium constant ($l\ mg^{-1}$)
K_R	Redlich-Peterson isotherm constant ($l\ g^{-1}$)
K_{FG}	Fowler-Guggenheim equilibrium constant ($l\ mg^{-1}$)
K_{FS}	Fritz-Schlunder(IIII) equilibrium constant ($l\ mg^{-1}$)
P_1	Weber-van Vliet constant
P_2, P_3,	Weber-van Vliet model exponent
P_4	
T	Absolute temperature (K)
W	Mass of adsorbent (g)
a_K	Khan model exponent
a_R	Redlich-Peterson isotherm constant ($l\ mg^{-1}$)
a_S	Sips equilibrium constant ($l\ mg^{-1}$)
a_T	Toth equilibrium constant
a_{RP}	Radke-Prausnitz maximum adsorption capacities ($mg\ g^{-1}$)
b_0	Baudu equilibrium constant
b_K	Khan constant
g	Redlich-Peterson isotherm exponent
k_f	Freundlich constant ($mg^{1-n}\ l^n\ g^{-1}$)
k_S	Sips maximum adsorption capacity ($mg\ g^{-1}$)

Table 7. Parameters

mFS	Fritz-Schlunder(III) model exponent
n	Koble-Corrigan model exponent
n^D	Dubinin-Astakhov model exponent
n_F	Freundlich constant
q_e	The equilibrium adsorption capacity of adsorbent (mg g^{-1})
q_{mB}	Baudu maximum adsorption capacity (mg g^{-1})
q_{mE}	Elovich maximum adsorption capacity (mg g^{-1})
q_{mFS}	Fritz-Schlunder(III) maximum adsorption capacity (mg g^{-1})
q_{SK}	Khan theoretical isotherm saturation capacity (mg g^{-1})
q_{mT}	Toth maximum adsorption capacity (mg g^{-1})
r_{RP}	Radke Prausnitz equilibrium constants
u	Jossens model exponent
x	Baudu model exponent
y	Baudu model exponent
z	Toth model exponent
α	Fritz-Schlunder(IV) model exponent
β	Fritz-Schlunder(IV) model exponent
θ_{DA}	Degree of micropore filling
θ_{FG}	Fractional coverage related to Fowler-Guggenheim model

1 cm^{-1} and appeared at 1087 cm^{-1}, which could be due to the interaction between the MCM-41 network and the copper oxide nanoparticles. These changes occur for two reasons: (1) confinement of nanoparticles within the MCM-41 network; or (2) the interaction between nanoparticles and MCM-41 networks. These interactions were performed by the electrostatic forces between the negative matrix and the nanoparticles. It was predicted that there will be strong interactions between the nanoparticles and negative networks [19,32]. The peak in the FTIR spectrum of the nanoparticles is not clear, so no new peak has been appeared in the infrared spectrum of the CuO/MCM-41 sample. However, the presence of nanoparticles in the lattice and their interactions with the MCM-41 lattice has led to all peaks specific to the MCM-41 spectrum have transmission, especially the main range (1086 cm^{-1}) is shiftef to higher wavelengths. On the other hand, the peak intensity is decreased in different areas [18].

BET/BJH Analysis

After investigating the adsorption and desorption of N_2 (Fig. 20), it was found that the hysteresis ring type A was formed. In type A hysteresis rings, the isotherms in which the adsorbed or desorbed branch slopes that were at average relative pressures, were related to two open capillary tubes. In this capillary with a polygonal cross-section where no

circular cross-section is required, the adsorbent along with the absorbed sides forms a cylindrical film of fluid. Information on the surface area, size, and radius of the pores are summarized in Table 4.

Isotherms Calculations

Using this paper data, all monolayer adsorption isotherms were calculated. The best isotherms in terms of error minimization and correlation maximization are given in Table 5.

CONCLUSIONS

Optimal amount version: The optimal version of the test accomplished with the maximum amount of pollutant treatment is shown in Table 6.

In order to oxidize and degrade the quinoline, the MCM-41 nanocomposite with CuO active component was synthesized by applying an easy method, and after that was characterized. The experiment was designed using DX software version 11, with no auxiliary oxidant intervention. The statistical results, the area of quinoline peaks, and the internal standard determined the residual quinoline concentration and indicated that the reaction was photocatalytic, and the degradation of the quinoline structure was oxidative. Along with increasing the catalyst, the highest yields of quinoline removal was obtained as 84%.

ACKNOWLEDGMENTS

This work was part of a Ph.D. thesis called “Design of optimized nanocatalyst for oxidation of quinoline and its derivatives”. The authors would like to thank Dr. Ghazaleh Chizari Fard for her assistance, and also are grateful from Nano Research and Technology Center of Islamic Azad University South Tehran Branch-Iran for their support.

REFERENCES

[1] Jukić, A., Petroleum refining and petrochemical processes. Natural Gas Composition, Classification, Processing, 2013.

[2] Chen, J.; De Crisci, A. G.; Xing, T., Review on catalysis related research at CanmetENERGY. *Can. J. Chem. Engin.* **2016**, *94*, 7-19, DOI: 10.1002/cjce.22322.

[3] Liew, K. Y.; Yee, A. H.; Nordin, M. R., Adsorption of carotene from palm oil by acid-treated rice hull ash. *J. Am. Oil Chemists' Soc.,* **1993** *70*, 539-541, DOI: 10.1007/BF02542590.

[4] Dahab, M. F.; Lee, Y. W.; Bogardi, I., A rule-based fuzzy-set approach to risk analysis of nitrate-contaminated groundwater. *Water Sci. and Technol.* **1994**, *30*, 45.

[5] Shamsaee, B. H.; Mehri, F.; Rowshanzamir, S.; Ghamati, M.; Behrouzifar, A., Desulfurization of benzothiophene from model diesel fuel using experimental (dynamic electroreduction) and theoretical (DFT) approaches. *Sep. Purif. Technol.* **2019**, *212*, 505-514, DOI: 10.1016/j.seppur.2018.11.057.

[6] Misra, P.; Badoga, S.; Chenna, A.; Dalai, A. K.; Adjaye, J., Denitrogenation and desulfurization of model diesel fuel using functionalized polymer: charge transfer complex formation and adsorption isotherm study. *Chem. Engin. J.* **2017**, *325*, 176-187, DOI: 10.1016/j.cej.2017.05.033.

[7] Ogunlaja, A. S.; Abdul-Quadir, M. S.; Kleyi, P. E.; Ferg, E. E.; Watts, P.; Tshentu, Z. R., Towards oxidative denitrogenation of fuel oils: Vanadium oxide-catalysed oxidation of quinoline and adsorptive removal of quinoline-N-oxide using 2,6-pyridine-polybenzimidazole nanofibers. *Arab. J. Chem.* **2017**, DOI: 10.1016/j.arabjc.2017.05.010.

[8] Babich, I. V.; Moulijn, J. A., Science and technology of novel processes for deep desulfurization of oil refinery streams: a review. *Fuel.* **2003**, *82*, 607-631, DOI: 10.1016/S0016-2361(02)00324-1.

[9] Abdel-Wahab, A. M. A.; Gaber, A. E. A. M., TiO_2-photocatalytic oxidation of selected heterocyclic sulfur compounds. *J. Photochem. Photobiol. A: Chem.* **1998**, *114*, 213-218., DOI: 10.1016/s1010-6030(98)00204-4.

[10] Baeza, P.; Aguila, G.; Gracia, F.; Araya, P., Desulfurization by adsorption with copper supported on zirconia. *Catal. Commun.* **2008**, *9*, 751-755, DOI: 10.1016/j.catcom.2007.08.020.

[11] Chester, A. W.; Derouane, E. G., Zeolite Characterization and Catalysis (Vol. 360). New York, EUA: Springer, 2009, pp. 327-329.

[12] Dotremont, C.; Vankelecom, I. F. J.; Morobe, M.; Uytterhoeven, J. B.; Vandecasteele, C., Zeolite-filled PDMS membranes. 2. Pervaporation of halogenated hydrocarbons. *J. Phys. Chem.B.* **1997**, *101*, 2160-2163, DOI: 10.1021/jp961809u.

[13] Vankelecom, I. F. J.; Dotremont, C.; Morobe, M.; Uytterhoeven, J. B; Vandecasteele, C., Zeolite-filled PDMS membranes. 1. Sorption of halogenated hydrocarbons. *J. Phys. Chem. B.* **1997**, *101*, 2154-2159, DOI: 10.1021/jp9618082.

[14] Cejka, J., Introduction to Zeolite Science and Practice. Elsevier, 2007, pp. 915-945.

[15] Botz, M. M., Overview of Cyanide Treatment Methods. Mining Environmental Management, Mining Journal Ltd., London, UK, 2001, 28-30.

[16] Zhang, Z. Y.; Shi, T. B.; Jia, C. Z.; Ji, W. J.; Chen, Y.; He, M. Y., Adsorptive removal of aromatic organosulfur compounds over the modified Na-Y zeolites. *Appl. Catal. B: Environ.* **2008**, *82*, 1-10, DOI: 10.1016/j.apcatb.2008.01.006.

[17] Zarrinabadi, E.; Abghari, R.; Nazari, A.; Mirjalili, M., Environmental effects of enhancement of mechanical and hydrophobic properties of polyester fabrics using silica/kaolinite/silver nanocomposite: A facile technique for synthesis and RSM optimization. *Eur. Asian J. Biosci.* **2018**, *12*, 437-450.

[18] Khanmoradi, M.; Nikoorazm, M.; Ghorbani-Choghamarani, A., Anchoring of Cu(II)-vanillin schiff base complex on MCM-41: A highly efficient and recyclable catalyst for synthesis of sulfides and 5-substituted 1H-tetrazoles and oxidation of sulfides to sulfoxides. *Appl. Organometallic Chem.* **2017**, *31*, e3693, DOI: 10.1002/aoc.3693.

[19] Nezamzadeh-Ejhieh, A.; Karimi-Shamsabadi, M., Comparison of photocatalytic efficiency of supported CuO onto micro and nano particles of zeolite X in photodecolorization of Methylene blue and Methyl orange aqueous mixture. *Appl. Catal. A: Gen.* **2014**, *477*, 83-92, DOI:10.1016/j.apcata.2014.02.031.

[20] Vaddi, D.; Subbarao, M. V.; Muralikrishna, M. P .S., Removal of calcium (Ca^{2+}) ion from aqueous solution by chemically activated thuja occidentalis leaves carbon (CATLC)-application for softening the groundwater samples. *Phys. Chem. Res.* **2019**, *7*, 449-466, DOI: 10.22036/pcr.2019.170974.1590.

[21] Jing, J.; Li, W.; Boyd, A.; Zhang, Y.; Colvin, V. L.; William, W. Y., Photocatalytic degradation of quinoline in aqueous TiO_2 suspension. *J. Hazard. Mater.* **2012**, *237*, 247-255, DOI: 10.1016/j.jhazmat.2012.08.037.

[22] Tegge, G., Hirayama, K.: Handbook of Ultraviolet and Visible Absorption Spectra of Organic Compounds (Handbuch der Ultravioletten und Sichtbaren Spektra Organischer Verbin-dungen). Plenum Press Data Division, a Division of Plenum Publishing Corporation, New York, NY, 1967. 642 Seiten, über 600 Tabellenseiten, 21× 28 cm, Preis $40, 00. Starch-Stärke: **1968**, 20, 278-278.

[23] Almasian, A.; Olya, M. E.; Mahmoodi, N. M.; Zarinabadi, E., Grafting of polyamidoamine dendrimer on polyacrylonitrile nanofiber surface: synthesis and optimization of anionic dye removal process by response surface methodology method. *Desalination and Water Treatment.* **2019**, *147*, 343-361, DOI: 10.5004/dwt.2019.23676.

[24] Zarrinabadi, E.; Abghari, R.; Nazari, A.; Mirjalili, M., Modeling and optimization of electromagnetic and saturated magnetic properties of polyester fabrics coated with Ag/kaolin/silica nanocomposites. *Bulgarian Chem. Commun.* **2018**, *50*, 154-167.

[25] Ghorbani-Choghamarani, A.; Nikpour, F.; Ghorbani, F.; and Havasi, F., xAnchoring of Pd(II) complex in functionalized MCM-41 as an efficient and recoverable novel nano catalyst in C-C, C-O and C-N coupling reactions using Ph3SnCl. *RSC Adv.* **2015**, *5*, 33212-33220, DOI: 10.1039/C5RA01934F.

[26] Kruk, M.; Jaroniec, M.; Kim, J. M.; Ryoo, R., Characterization of highly ordered MCM-41 silicas using X-ray diffraction and nitrogen adsorption. *Langmuir.* **1999**, *15*, 5279-5284, DOI: 10.1021/la990179v.

[27] Brazlauskas, M.; Kitrys, S., Synthesis and properties of CuO/Zeolite sandwich type adsorbent-catalysts. *Chinese J. Catal.* **2008**, *29*, 25-30, DOI: 10.1016/S1872-2067(08)60013-3.

[28] Covarrubias, C., Gracia, F.; Palza, H., Catalytic degradation of polyethylene using nanosized ZSM-2 zeolite. *Appl. Catal. A: Gen*. **2010**, *384*, 186-191, DOI: 10.1016/j.apcata.2010.06.034.

[29] Castagnola, N. B.; Dutta, P. K., Nanometer-sized zeolite X crystals: Use as photochemical hosts. *J. Phys. Chem. B*. **1998**, *102*, 1696-1702, DOI: 10.1021/jp980103s.

[30] Kantam, M. L.; Rao, B. P.; Choudary, B. M.; Rao, K. K.; Sreedhar, B.; Iwasawa, Y.; Sasaki, T., Synthesis of nanocrystalline zeolite beta in supercritical fluids, characterization and catalytic activity. *J. Mol. Catal. A: Chemical.* **2006**, *252*, 76-84, DOI: 10.1016/j.molcata.2006.02.044.

[31] Chung, J. S.; Yun, H. G.; Koh, D. J.; Kim, Y. G., Preparation and Fischer-Tropsch reaction of highly-reduced cobalt clusters in cobalt-exchanged zeolite. *J. Mol. Catal.* **1993**, *79*, 199-215, DOI: 10.1016/0304-5102(93)85102-Y.

[32] Salavati-Niasari, M.; Sobhani, A., Ship-in-a-bottle synthesis, characterization and catalytic oxidation of cyclohexane by Host (nanopores of zeolite-Y)/guest (Mn(II), Co(II), Ni(II) and Cu(II) complexes of bis (salicyaldehyde) oxaloyldihydrazone) nanocomposite materials. *J. Mol. Catal. A: Chemical.* **2008**, *285*, 58-67, DOI: 10.1016/j.molcata.2008.01.030.

[33] Saadi, R.; Saadi, Z.; Fazaeli, R.; Fard, N. E., Monolayer and multilayer adsorption isotherm models for sorption from aqueous media. *Korean J. Chem. Engin*. **2015**, *32*, 787-799, DOI: 10.1007/s11814-015-0053-7.